Published in final edited form as:
Appl Catal B. 2018 June 5; 225: 91–99. doi:10.1016/j.apcatb.2017.11.058.

Heterogeneous activation of persulfate by reduced graphene oxide–elemental silver/magnetite nanohybrids for the oxidative degradation of pharmaceuticals and endocrine disrupting compounds in water

Chang Min Park[a,b], **Jiyong Heo**[c], **Dengjun Wang**[b], **Chunming Su**[d], **Yeomin Yoon**[e]

[a]Department of Environmental Engineering, Kyungpook National University, 80 Daehak-ro, Buk-gu, Daegu, 41566, South Korea

[b]National Research Council Research Associate at the U.S. Environmental Protection Agency, 919 Kerr Research Drive, Ada, OK 74820, USA

[c]Department of Civil and Environmental Engineering, Korea Army Academy at Youngcheon, 495 Hogook-ro, Gokyungmeon, Youngcheon, Gyeongbuk 38900, South Korea

[d]Groundwater, Watershed and Ecosystem Restoration Division, National Risk Management Research Laboratory, Office of Research and Development, U.S. Environmental Protection Agency, 919 Kerr Research Drive, Ada, OK 74820, USA

[e]Department of Civil and Environmental Engineering, University of South Carolina, 300 Main Street, Columbia, SC 29208, USA

Abstract

Reduced graphene oxide hybridized with zero-valent silver and magnetite nanoparticles (NPs) (rGO-Ag^0/Fe_3O_4 nanohybrids) prepared via *in situ* nucleation and crystallization was used to activate peroxydisulfate (PDS) for degradation of pharmaceuticals and endocrine disrupting compounds (phenol, acetaminophen, ibuprofen, naproxen, bisphenol A, 17β-estradiol, and 17α-ethinyl estradiol). The deposition of Ag^0 and Fe_3O_4 in rGO nanosheet enhanced the catalytic removal of phenol in the heterogeneous activation of PDS. The adsorption capacities of rGO-Ag^0/Fe_3O_4 for 10 μM phenol were 1.76, 1.33, and 2.04 μmol g^{-1}-adsorbent at pH 4, 7, and 10, respectively, which are much higher than those of single NPs studied (Ag^0, nanoscale zero-valent iron, and rGO). The rGO-Ag^0/Fe_3O_4 effectively activated PDS to produce strong oxidizing SO_4·and facilitate an electron transfer on the surface of the nanohybrid. The initial pseudo-first-order rate (k_{ini}) constant for phenol degradation in PDS/rGO-Ag^0/Fe_3O_4 system was 0.46 h^{-1} at pH 7, which is approximately eight times higher than that in the presence of single NPs (k_{ini} = 0.04–0.06 h^{-1}) due to the synergistic effects between adsorption and catalytic oxidation. Among various organic contaminants tested, the simultaneous use of rGO-Ag^0/Fe_3O_4 (0.1 g/L) and PDS (1 mM) achieved more than 99% degradation of acetaminophen and 17β-estradiol at pH 7. The radical scavenging studies with methanol and natural organic matter indicated that phenol was

*Corresponding authors. su.chunming@epa.gov (C. Su), yoony@cec.sc.edu (Y. Yoon).

Appendix A. Supplementary data
Supplementary data associated with this article can be found, in the online version, at http://dx.doi.org/10.1016/j.apcatb.2017.11.058.

more likely to be degraded via free $SO_4\cdot^-$ and ·OH formation or a non-radical oxidative pathway. Our findings indicate that the rGO-Ag^0/Fe O nanohybrids can be used as an efficient magnetically-separable nanocatalyst for removal of organic compounds in water and wastewater treatment.

Graphical Abstract

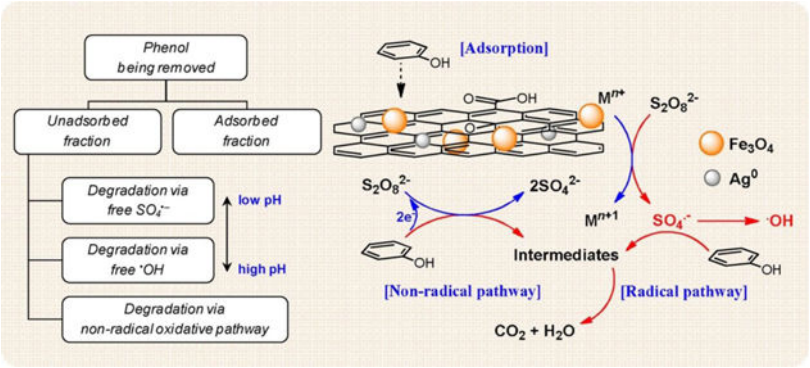

Keywords

Heterogeneous activation; Peroxydisulfate; Nanohybrid; Phenol; Sulfate radicals

1. Introduction

Sulfate radical ($SO_4\cdot^-$ redox potential of 2.5–3.1 V), a strong one-electron oxidant, has attracted increasing attention due to its high efficiency and selectivity for the catalytic degradation of refractory organic contaminants and algal toxins (phenol, benzoic acid, 4-chlorophenol, and microcystin-LR) [1–4]. Generally, $SO_4\cdot^-$ precursors, persulfate (PS) (*i.e.*, peroxymonosulfate (PMS, SO_5^{2-}) or peroxydisulfate (PDS, $S_2O_8^{2-}$)) can be activated effectively by external energy (*e.g.*, heat [5], ultraviolet (UV) [6], ultrasound [7], and radiolysis [8]) or transition metal catalysts (*i.e.*, M^{n+} = Ag(I), Ce(III), Co(II), Fe (II), Fe(III), Mn(II), Ni(II), Ru(III), and V(III)) [9] to produce $SO_4\cdot^-$ in a photochemical, thermal, or chemical processes. The transition metals require much less energy and consumable chemicals for $SO_4\cdot^-$ generation compared with those using different energy activators [9]. For example, PMS can be activated by transition metals via the following two pathways (Eqs. (1) and (2)):

$$HSO_5^- + M^{n+} \rightarrow M^{(n+1)+} + SO_4\cdot^- + OH^- \quad (1)$$

The hydroxyl radical (OH) may be formed during PMS activation, in Eq. (2):

$$HSO_5^- + M^{n+} \rightarrow M^{(n+1)+} + SO_4^{2-} + \cdot OH \quad (2)$$

Similarly, $SO_4\cdot^-$ can be generated by transition metals via activation of PDS, as follows:

$$S_2O_8^{2-} + M^{n+} \rightarrow M^{(n+1)+} + SO_4^{\cdot -} + SO_4^{2-} \quad (3)$$

$$SO_4^{\cdot -} + M^{n+} \rightarrow M^{(n+1)+} + SO_4^{2-} \quad (4)$$

$$S_2O_8^{2-} + 2M^{n+} \rightarrow 2M^{(n+1)+} + 2SO_4^{2-} \quad (5)$$

A systematic study of several transition metal–PS/H_2O_2 couples for their reactivity toward degradation of a model organic substrate (2,4-dichlorophenol) showed that Ag(I) was the best activator for PDS in generating freely diffusible $SO_4^{\cdot -}$ (Eq. (3)), whereas Co(II) was the most effective for activating PMS [9]. It was also found that metal-bound (or caged) $SO_4^{\cdot -}$ may be produced with homogeneous Ag(I)/$K_2S_2O_8$ coupling reagent:

$$S_2O_8^{2-} + Ag^{+} \rightarrow \left[Ag^{II}(SO_4\cdot)\right]^{+} + SO_4^{2-} \quad (6)$$

Although dissolved Ag(I)/Co(II) was highly effective in producing $SO_4^{\cdot -}$ in the activation of PS, the toxicity associated with dissolved metals is always a big concern in water and wastewater treatment. Alternatively, iron compounds (e.g., pyrite (FeS_2) [10], magnetite (Fe_3O_4) [11], core-shell Fe–Fe_2O_3 [12], or spinel-type ferrite (MFe_2O_4, M = Mn, Fe, Co, Ni, and Cu) [13]) have received great attention in a heterogeneous manner that immobilizes iron in support materials due to their excellent capabilities for PS activation and intrinsic magnetic properties, which facilitates easy phase-separation by simply using a magnet. However, excess feeding or sequential additions of Fe(II) can also play a role in quenching the formation of $SO_4^{\cdot -}$, whereas Fe(II) is rapidly oxidized to Fe(III) (Eq. (4)). The zero-valent iron (ZVI, Fe^0) can overcome these disadvantages by slowly releasing Fe(II) in water [14,15], but the rapid aggregation of ZVI induced by its magnetic property reduces the catalytic activity [16]. Carbon-based nanomaterials (CNMs) (e.g., carbon nanotubes [17,18] and graphene oxide (GO) [19–21]) have also been suggested as alternative catalysts as well as being excellent electron transfer mediators for organic compound oxidation in a heterogeneous PS activation system. Recently, the incorporation of metal/metal oxides nanoparticles (NPs) on CNMs has been explored as futuristic and cost-effective (photo)catalysts. Those nanohybrid (NH) materials are designed for synergistic effects between (photo)catalysis and the adsorption of organic contaminants or heavy metal ions [22]. Additionally, a lower aggregation propensity of NHs increases the overall specific surface area of the nano-catalysts, thus enhancing their performance in contaminant removal [23].

Among many CNMs, graphene and its derivatives have been used extensively to support metal/metal oxide NPs for the construction of graphene-based NHs due to their high electrical conductivity, chemical/mechanical stability, and large specific surface area and reactivity [24,25]. The hybridization of graphene with metal/metal oxide NPs can improve robustness against target contaminants and inhibit the corrosion/leaching of metal ions, which enhances the life span of the catalysts. Moreover, the delocalized π-electron systems

of graphene renders a strong adsorption capacity for organic compounds by π-π stacking interactions [26]. There have been several attempts to improve the (photo)catalytic activity by controlling the composition of magnetic cobalt ferrite NPs [27] or combining graphene with various metal/metal oxides NPs. For example, Al-Anazi et al. [27] reported that the increase in molar ratio of cobalt in the spinel ferrite NPs ($Co_xFe_{3-x}O_4$; x = 0.1, 0.5, 0.7, 1.0) enhanced the degradation efficiency of 2-phenylbenzimidazole-5-sulfonic acid in activation of PMS into reactive $SO_4\cdot^-$ and ·OH without use of additional heat and light. P25, titanate nanotubes [28], ZnO [29], CuO [30]/Cu_2O [31], $CuFe_2O_4$ [32], and Bi_2WO_6 [33] have been assembled with graphene nanosheets as photocatalysts for organic dye removal. More recently, several facile approaches for synthesis of reduced graphene oxide (rGO)-based NHs with Mn_3O_4 [34], Co_3O_4 [35], $Co(OH)_2$ [36], $MnFe_2O_4$ [37], and $CoFe_2O_4$ [38] have been demonstrated to enhance the catalytic performance in heterogeneous activation of PMS system for degradation of organic dyes (e.g., methyl violet, methyl orange, methylene blue, orange II, and rhodamine B) or phenols. To our knowledge, there is no reported study examining bimetallic rGO NH (silver and iron compounds deposited on a rGO nanosheet) as a heterogeneous PDS catalyst in degradation of organic contaminants, although those single metal/metal oxides have been found to be very efficient catalyzers for $SO_4\cdot^-$ formation in PS activation systems.

Over the past few years, large groups of environmental contaminants such as pharmaceuticals and endocrine disrupting compounds (EDCs) have gained much attention because they are frequently detected at trace levels (< 0.1 μg/L) in surface water and wastewater [39–41]. Particularly, the pharmaceuticals and EDCs occurring in surface and ground waters are likely to have adverse impacts and potential risks to human health and ecology but are not commonly regulated [42]. In the current study, we tested the catalytic activity of rGO hybridized with zero-valent silver and magnetite (rGO-Ag^0/Fe_3O_4) in the heterogeneous activation of PDS for the catalytic removal of phenol, acetaminophen, ibuprofen, naproxen, bisphenol A (BPA), 17β-estradiol (E2), and 17α-ethinyl estradiol (EE2). Specific objectives of this study were to provide the degradation efficiency of organic pollutants and insights into the mechanisms of phenol removal, including the possible involvement of reactive oxidizing species on the NH. The performance of rGO-Ag^0/Fe_3O_4 was also compared with that of single (*i.e.*, AgNP, nanoscale zero-valent iron (NZVI), and rGO) in the activation of H_2O_2. Our group recently synthesized the rGO-Ag^0/Fe_3O_4 NH to investigate the aggregation kinetics and long-term stability under environmentally relevant conditions [43]. It was found that bimetallic rGO NH (rGO-Ag^0/Fe_3O_4) showed excellent stability over a wide range of pH, type of electrolytes, and ionic strength (IS) conditions. We systematically characterized this highly stable NH and identified removal pathways for in-depth understanding of the mechanisms involved in the catalytic removal of organic compounds.

2. Experimental

2.1 Material preparation

A modified Hummers method was used to prepare GO [44]. The method involves the oxidative treatment of natural graphite flakes (3061 grade, Asbury Graphite Mills) with

concentrated sulfuric acid and oxidizing agents followed by centrifugation, ultrasonication, washing, and separation via membrane filtration. A detailed description of the procedure is provided in the Supplementary Information. Phenol, acetaminophen, ibuprofen, naproxen, BPA, E2, and EE2 were purchased from Sigma-Aldrich Co. with purity higher than 98%. The physicochemical properties and chemical structures of the target organic compounds investigated are listed in Table S1. Suwannee River humic acid (SRHA, Standard II) and fulvic acid (SRFA, Standard II) were obtained from the International Humic Substances Society and were used as radical scavengers. Other chemicals used in this study (*i.e.,* $NaNO_3$, $KMnO_4$, CH_3OH, $Na_2S_2O_3$, $K_2S_2O_8$, H_2O_2, H_2SO_4, HCl, and NaOH obtained from Sigma-Aldrich Co.) are of reagent grade. All solutions were prepared in ultra-pure water (> 18 MΩ/cm) obtained from a Milli-Q water purification system (Millipore Co.).

2.2 Characterization of rGO-based nanohybrids

The size and morphology of the synthesized rGO and rGO-Ag^0/Fe_3O_4 NH were characterized by field-emission transmission electron microscopy (FE-TEM; Titan G2 with ChemiSTEM Cs Probe; FEI). X-ray photoelectron spectroscopy (XPS) of rGO and rGO-Ag^0/Fe_3O_4 NH were obtained using a PHI Quantera SXM scanning X-ray microscope (ULVAC-PHI, Inc.). The structural properties of graphite, rGO, and rGO-Ag^0/Fe_3O_4 NH were examined using a Rigaku Miniflex II X-ray diffractometer with Mn-filtered Fe Kα radiation (λ = 0.1937 nm), operated at 30 kV and 15 mA. Powder X-ray diffraction (XRD) patterns were recorded from 2θ of 2° to 90° in 0.02° step increments, and the peaks of the collected XRD patterns were analyzed with the software package, Jade (Materials Data, Inc.) which allows data comparison with the JCPDS Powder Diffraction File database. The surface functional groups of rGO and rGO-Ag^0/Fe_3O_4 NH were identified by Fourier transform-infrared (FT-IR) spectrometer (Thermo Scientific Nicolet 6700) in the wavenumber range of 400–4000 cm^{-1}. UV–vis spectra of AgNP (Sigma-Aldrich Inc.), rGO, and rGO-Ag^0/Fe_3O_4 NH were recorded on a Lambda 35 UV–vis spectrophotometer (Perkin-Elmer) in the wavelength range of 200–900 nm.

2.3 Catalytic degradation experiments

The degradation experiments in heterogeneous activation of PDS and H_2O_2 were conducted in duplicate in 60 mL amber glass bottles containing 10 μM of phenol and other organic contaminants (*i.e.*, acetaminophen, ibuprofen, naproxen, BPA, E2, and EE2). The bottles were covered completely with aluminum foil to avoid potential photodegradation during the reaction processes. To initiate the catalytic reaction, 1 mM PDS or H_2O_2 were added to the solution. At predetermined time intervals, 1 mL aliquot of the sample was withdrawn, and the reaction was immediately quenched by adding 0.5 M $Na_2S_2O_3$ solution to the mixture. The NPs were then removed by high-speed centrifugation (18,000*g*) for 15 min followed by filtration (0.45-μm filter membrane (VWR, USA). The filtrates were loaded on to a high-performance liquid chromatography (HPLC) system (Hewlett Packard, Agilent 1100) for all chromatographic analyses of organic compounds, which were measured using a C18 column (Zorbax Eclipse XDB-C18, 150 × 4.6 mm^2; i.d. 5 μm) coupled to a compatible guard column with HPLC-grade mobile phase reagents (acetonitrile/methanol) and water at a flow rate of 0.5–1 mL/min. The UV-vis-diode array detector was set at 254 nm for acetaminophen and 210 nm for ibuprofen [45]. A HPLC-fluorescence detector method was used to detect

phenol, naproxen, BPA, E2, and EE2. The initial degradation rate constants (k_{ini}) were calculated by a pseudo-first-order kinetic model for the first 1 h of reaction (Tables S2 and S3). The quenching experiments were also conducted to determine the radical ($SO_4\cdot^-$) scavenging effects using methanol (100 mM), SRHA (10 mg/L), and SRFA (10 mg/L) in heterogeneous PDS/rGO-Ag^0/Fe_3O_4 system.

2.4 Adsorption

Prior to the degradation reaction described above, batch kinetic experiments were carried out at 298 K to determine the kinetic parameters for the adsorption of phenol (10 μM) on the ultrasonically dispersed AgNP, NZVI (Nanoiron Inc.), rGO, and rGO-Ag^0/Fe_3O_4 (0.1 g/L) at a sonication bath with an output of 70 W at a frequency of 42 kHz (Branson 1510 sonicator) for 30 min. The pH of the solution was adjusted to 4, 7, and 10 using 0.001–0.1 M HCl and NaOH solutions. A small volume of samples was taken from the solution at predetermined time intervals with continuous stirring for 6 h, and then diluted 10 times to obtain a total volume of 10 mL. The supernatants were immediately centrifuged (18,000*g*) for 15 min and filtered through the 0.45-μm pore size filter membrane to remove residual particulates. Phenol concentration was determined by a HPLC system. The experiments were performed in triplicates.

3. Results and discussion

3.1 Properties of nanoparticles

The morphology and structures of rGO and rGO-Ag^0/Fe_3O_4 NH were observed by FE-TEM. The elemental mapping results in Figs. 1 and S1 show that Ag^0 and Fe_3O_4 NPs were deposited directly on the surfaces of rGO by *in situ* nucleation and crystallization; the diameters of Ag^0 and Fe_3O_4 NPs were observed to be 50–200 nm. It can be clearly seen that the rGO layers of its NHs have several wrinkles due to extremely thin layers (~1 nm thick) [46,47]. The surface of rGO-Ag^0/Fe_3O_4 NH showed a high degree of entanglement (fluffy sphere-like structure) but less aggregation (effective diameters of 220–300 nm than rGO (400–710 nm).

The crystal structures of rGO and rGO-Ag^0/Fe_3O_4 NH were identified by their characteristic peaks in the XRD patterns (Fe K_α radiation; Fig. 2(a)). A strong diffraction peak of rGO with a *c*-axis interlayer spacing (d) of 3.45 Å at 32.6° (2θ) corresponds to the (002) crystalline plane of graphite (JCPDS No. 01-089-8487), indicating high crystallinity of the pristine graphite. XRD patterns of rGO-Ag^0/Fe_3O_4 NH showed a relatively small diffraction peak of graphite centered at 33.1° (2θ; interlayer spacing of 3.40 Å), which may be ascribed to compressive loading of silver ions on rGO and a reduction effect [48]. Instead, three other crystalline phases of Ag^0-3C, *syn* (JCPDS No. 01-087-0597) were observed for those NHs at 48.5, 56.6, and 84.1° (2θ) with d = 2.36, 2.04, and 1.44 Å, which, respectively, indexed as the (111), (200), and (220) faces. The rGO-Ag^0/Fe_3O_4 NH showed a broad diffraction peak at 45.5° (2θ) with d = 2.50 Å, indexed to the (311) planes of magnetite crystal (Fe_3O_4, JCPDS No. 01-075-0449).

Variations in the surface functional groups of rGO and rGO-Ag^0/Fe_3O_4 NH were analyzed via FT-IR spectroscopy (Fig. 2b). The strong peaks of rGO at 1402, 1173, and 877 cm^{-1} corresponded to aliphatic C-H bending, C-O-C stretching, and aromatic C-H bending vibration, respectively. The sharp absorption peaks of rGO-Ag^0/Fe_3O_4 NH at around 1633 and 1538 cm^{-1} could be ascribed to the C=C and C=O stretching vibrations, respectively [49,50]. The weak peaks at 3300 and 2926 cm^{-1} were assigned to O-H and C-H stretching vibrations. Many peaks in the fingerprint regions between 1600 and 660 cm^{-1} for rGO moved to peaks around 1800–1100 cm^{-1} for rGO-Ag^0/Fe_3O_4 NH due to the deposition of Ag^0 and Fe_3O_4 on rGO nanosheet.

Fig. 2c shows the UV–vis diffuse reflectance spectra of the AgNP, rGO, and rGO-Ag^0/Fe_3O_4 NH. NZVI did not exhibit any obvious absorbance peak (data not shown) [51]. The surface plasmon resonance band of the Ag^0 NPs was observed at 436 nm [52]. The absence of absorption peak of rGO-Ag^0/Fe_3O_4 NH in the visible region indicates that Ag^0 NPs are fully wrapped by the negatively charged rGO sheets, which also caused little shift in the maximum absorption peak position with a similar spectral shape of rGO by the deposition of Ag^0 and Fe_3O_4 NPs (rGO-Ag^0/Fe_3O_4 NH) on rGO.

XPS was used to confirm the chemical compositions of rGO and rGO-Ag^0/Fe_3O_4 NH. A wide survey scan of C1 s and O1 s spectra was taken in the range of binding energy (BE), 0–800 eV (Fig. 3a). No extra peak was observed, ruling out any impurities other than C, O, Ag, and Fe elements. Table S2 shows C1 s and O1 s XPS curve fitting results of rGO and rGO-Ag^0/Fe_3O_4 NH. The strong C1 s peak of rGO at 284.3 eV assigned to non-oxygenated (aromatic) carbon (C-C/C=C), decreased appreciably, whereas peaks of rGO-Ag^0/Fe_3O_4 NH at 286.1 and 288.8 eV, assigned to epoxy or hydroxyl carbon, C-O and carboxylate carbon, COO^-, respectively, arose when Ag^0 and Fe_3O_4 NPs were deposited on rGO [53]. Other peaks at 287.0–287.8 eVs correspond to carbons attached to different O-containing moiety, C=O. The deconvolution of the wide and asymmetric O1 s peak showed that a main peak of rGO (77.4%) at 532.2 eV was attributed to carbonyl and carboxyl oxygen (C=O). The weakest O1 s peak (1.45%) occurred at 530.0 eV, which was assigned to a quinone-type oxygen (COO^-/C=O). The rGO-Ag^0/Fe_3O_4 NH showed reduced O1 s peaks (21.4%) at 532.4 eV, but their O1 s peaks at 530.2 eV increased significantly to 49.0% [54]. These peak shifts, by 1.8–2.0 eVs, towards lower BE indicated higher exposure to oxygen during the chemical reductive synthesis of NH. The notable peaks of rGO-Ag^0/Fe_3O_4 at 368.2 and 374.2 eV in Ag3d region of high-resolution XPS curve (Fig. 3(d)) result from Ag $3d_{5/2}$ and Ag $3d_{3/2}$, respectively due to a strong interaction of Ag core with the carboxyl oxygen (C=O) [55]. This result indicates that silver is deposited on rGO surface in metallic form (Ag^0). The other two peaks centered at 367.4 and 368.8 eV reveal little contribution to AgO and Ag^+, respectively. The main peaks of centered at 710.7–711.9 (including satellite peak at 718.2 eV) and 724.0 eV (including satellite peaks at 728.6 and 733.9 eV) in Fe2p region of XPS spectra (Fig. 3(e)) are expected to the binding energy of $Fe2p_{3/2}$ and $Fe2p_{1/2}$, respectively, which corresponds to Fe^{3+} state of magnetite [56]. Overall, the deposition of Ag^0 and Fe_3O_4 NPs on rGO sheet (rGO-Ag^0/Fe_3O_4 NH) has enhanced surface reactivity and the surface site availability of NH due to the incorporation of the transition metals and reduced NP aggregation. In addition, the stronger peak (C-O) at 286.1 eV and lower C/O

atomic ratio of NH may cause higher adsorption capacity via Lewis acid-base or π–π interaction

3.2. Activation of PDS and H_2O_2 with rGO nanohybrid for phenol degradation

PDS or H_2O_2 alone was nonreactive towards phenol degradation during 6 h of reaction (Fig. S2). In Figs. 4 and S3, the activation efficiencies of PDS and H_2O_2 by the four NPs (*i.e.*, AgNP, NZVI, rGO, and rGO-Ag^0/Fe_3O_4) were compared for the catalytic degradation of phenol at pH 4, 7, and 10. The control experiments were also performed using the two single metallic rGO NHs (*i.e.*, rGO-Ag^0 and rGO-Fe_3O_4) with PDS and H_2O_2 (data not shown). In the presence of different NPs, when PDS or H_2O_2 was introduced in the heterogeneous activation systems, the decomposition of PDS or H_2O_2 occurred immediately either in the suspension or on the surface of NPs, although complete phenol removal was not achieved within 6 h (Figs. 4, S2, and S3). As water molecules ($E°$(·OH/H_2O) = +2.80 V/NHE) cannot be oxidized thermodynamically by PDS/H_2O_2 alone ($E°$($S_2O_8^{2-}$/SO_4^{2-}) = +2.01 V/NHE and $E°$(H_2O_2/H_2O) = +1.78 V/NHE) [2], the catalytic reduction of PDS/H_2O_2 via direct one/two-electron transfer will only occur on the surface of highly reactive NPs.

Among the six NPs examined including control experiments, rGO-Ag^0/Fe_3O_4 showed the highest removal efficiency towards phenol in the activation of PDS at all pH values. The k_{ini} values for rGO-Ag^0/Fe_3O_4 at pH 4, 7, and 10 were 0.67, 0.46, and 0.23 h^{-1} in PDS and 0.10, 0.04, and 0.10 h^{-1} in H_2O_2, respectively. This is due to synergistic effect between higher adsorption of phenol (described below) and greater catalytic oxidation in activation of PDS than H_2O_2. In the catalytic activation of PDS and H_2O_2, the reaction rates of phenol removal under an acidic condition (pH 4) were higher than those under neutral and basic conditions (pH 7 and 10; Table S3). The less negative charge of NPs resulting from protonation of the hydroxyl groups under acidic condition (pH 4) will decrease the electrostatic repulsive force between PDS/H_2O_2 and the surface sites of NPs, promoting the removal of phenol in the suspension [57]. Liang and Su demonstrated, using a chemical probe method to thermal activation of PS, that $SO_4{\cdot}^-$ were dominant species under acidic conditions, whereas the amount of ·OH increased to co-exist in the aqueous solution as the pH increased [58]. The $SO_4{\cdot}^-$ radical can be converted into the ·OH by undergoing reactions with hydroxyl OH^- ions in the alkaline pH range (Eq. (7)) or with water molecules at any pH value (Eq. (8)) [59]. The ·OH formed at higher pH acts as a $SO_4{\cdot}^-$ scavenger, to be reconverted to SO_4^{2-} ions (Eq. (9)), which will reduce the degradation rate of organic compounds under neutral/basic conditions in the PDS/rGO-Ag^0/Fe_3O_4 system.

$$SO_4{\cdot}^- + OH^- \rightarrow SO_4^{2-} + \cdot OH(\text{alkaline pH}) \quad (7)$$

$$SO_4{\cdot}^- + H_2O \rightarrow HSO_4^- + \cdot OH(\text{any pH}) \quad (8)$$

$$SO_4{\cdot}^- + \cdot OH \rightarrow SO_4^{2-} + OH^- (\text{recombination}) \quad (9)$$

Thus, the reduced freely diffusible $SO_4{\cdot}^-$ at high pH will decrease the degradation efficiency of phenol. This suggests that the pH-dependent surface charge of NPs would likely determine the reactivity for the adsorption as well as degradation of phenol via a radical-mediated oxidation. It was also found that 47% of phenol was removed with a PDS/rGO-Ag^0/Fe_3O_4 coupled process (k_{ini} = 0.46 h^{-1}) at a neutral pH, whereas 17% was removed in the activation of H_2O_2 (k_{ini} = 0.04 h^{-1}). These results indicate that $SO_4{\cdot}^-$ play a more important role in degradation of phenol than ·OH.

3.3. Adsorption kinetics of phenol on rGO nanohybrid

To further quantify the role of the adsorption on the catalytic removal of phenol, phenol uptake by the four NPs was determined at pH 4, 7, and 10 prior to 6 h of degradation reaction (Figs. 5 and S4). The kinetic adsorption data were described using the pseudo-second-order kinetic model given in Eq. (10) [60,61], and the kinetics parameters of phenol adsorption are listed in Table S4.

$$\frac{dq_t}{dt} = k(q_e - q_t)^2 \tag{10}$$

which can be written as Eq. (11).

$$\frac{t}{q_t} = \frac{1}{kq_e^2} + \frac{t}{q_e} \tag{11}$$

where q_t and q_e (=$(C_0 - C_e)V/m$) are the amounts of phenol adsorbed at time t and at equilibrium state (μmol/g-adsorbent), k is the apparent adsorption rate constant (g-adsorbent/μmol h), V is the volume of suspension (L), and m is the mass of dry adsorbent (g). As shown in Figs. 5a, S4a, and S4c, the adsorption capacity of NPs increased in the order of rGO-Ag^0/Fe_3O_4 > rGO > NZVI ≥ AgNP. The rGO-based NPs exhibited a higher adsorption efficiency of phenol than that of the other two NPs because of the unique property of rGO nanosheets (one-atom-thick thick two-dimensional structure) with sp^2 hybridized carbon atoms, which facilitates direct contact with phenol via strong π–π interaction [62]. The rGO-Ag^0/Fe_3O_4 NH showed at least 1.3 times higher adsorption efficiency of phenol than that of rGO (1.76, 1.33, and 2.04 μmol/g-adsorbent for rGO-Ag^0/Fe_3O_4 and 1.08, 0.86, and 1.51 μmol/g-adsorbent for rGO at pH 4, 7, and 10, respectively), indicating that the hybridization with Ag^0 and Fe_3O_4 on rGO increased the adsorption capacity. This also indicates that the higher adsorption capacity of rGO-Ag^0/Fe_3O_4 toward phenol is not positively correlated to the π–π interaction because the degree of reduction of rGO was higher than rGO-Ag^0/Fe_3O_4 (the atomic ratio of C/O = 4.8 for rGO and 1.3 for rGO-Ag^0/Fe_3O_4 as confirmed by XPS analysis). It is instead attributed to the following two aspects: (i) the deposition of Ag^0 and Fe_3O_4 on rGO nanosheets reduces the nanoparticle aggregation [43]; making more reactive surface sites available for phenol adsorption. Assembling magnetic iron oxide (*e.g.*, magnetite) into rGO provides magnetic attraction, which promotes particle aggregation between rGO-Fe_3O_4 NHs [43]. However, the bimetallic rGO NH with zero-valent silver and magnetite showed smaller hydrodynamic sizes (D_h) over a wide range of pH, type of cations, and ISs due to a higher electrostatic repulsion by rGO NHs edge–edge interactions in the aquatic environment. (ii) the higher occupying epoxy or hydroxyl

groups of rGO-Ag^0/Fe_3O_4 (17.6%) than rGO (12.5%) can act as more Lewis base sites responsible for the formation of chemical bonding with phenolic hydroxyl group of phenol[53].

The total amount of phenol removed by the four NPs as well as the percentage of adsorption and oxidation were calculated in Table S5. There was a noticeable oxidation (85.4%), particularly under acidic conditions (pH 4), in the PDS/rGO-Ag^0/Fe_3O_4 system following a higher amount of adsorption (14.6%) observed with rGO-Ag^0/Fe_3O_4. Similarly, rGO-Ag^0/Fe_3O_4 NH in catalytic activation of H_2O_2 exhibited greater oxidative degradation of phenol than that of single NPs under acidic/neutral conditions (pH 4 and 10), but the oxidation performance was much lower than PDS at all pH values tested. This confirmed that rGO-Ag^0/Fe_3O_4 was responsible for enhanced activation of PDS on the surface of the NH (via non-radical oxidative pathway in which the organic compounds are oxidized by donating electrons to PDS/H_2O_2 on NPs) or in suspension to produce free $SO_4{\cdot}^-$ and ·OH. In contrast, NZVI is much stronger in activating H_2O_2 to form ·OH under acidic and neutral conditions (12.1 and 5.26% of phenol removal at pH 4 and 7, respectively) than PDS (6.04 and 5.21% at pH 4 and 7, respectively), whereas rGO was more active for H_2O_2 activation under acidic conditions (15.4% at pH 4) than PDS (12.8% at pH 4). This is the first study reporting the high efficiency of rGO-Ag^0/Fe_3O_4 NH in the heterogeneous activation of PDS, promoting the catalytic oxidation of phenol. In this study, we also undertook further investigations of selectivity towards various organic compounds, degradation kinetics, and mechanisms for evaluating the potential of the PDS/rGO-Ag^0/Fe_3O_4 system in the removal of organic pollutants.

3.4. Selectivity of the PDS/rGO-Ag^0/Fe_3O_4 NH oxidation system

Fig. 6 shows the oxidative degradation kinetics of selected organic compounds (*i.e.*, acetaminophen, ibuprofen, naproxen, BPA, E2, and EE2 (Table S1)) in the PDS/rGO-Ag^0/Fe_3O_4 system. In contrast to low substrate-dependent reactivity under acidic conditions (pH 4), substrate specific-reactivity was evident under neutral/basic conditions (pH 7 and 10). Significant degradation (> 90% in 1 h of reaction) of acetaminophen, ibuprofen, E2, and EE2 and moderate degradation of naproxen and BPA (50–90% in 1 h reaction) were observed under acidic conditions (pH 4). However, ibuprofen and EE2 showed moderate degrees of degradation under neutral/basic conditions (pH 7 and 10), whereas a low level of degradation (< 50% in 1 h reaction) was observed for naproxen and BPA (k_{ini} = 0.45 and 0.35 h^{-1} for naproxen and BPA, respectively) during 6 h of oxidative reaction. BPA has been considered as a well-known refractory pollutant that is not effectively degraded in Fenton-like processes, even though the engineered NMs (*e.g.*, AgNP and NZVI) are present under neutral/basic conditions [63]. The electro-oxidation of BPA generally requires a two-electron transfer process, which may retard the catalytic degradation of BPA [64].

Although the active $SO_4{\cdot}^-$ species tend to be rapidly quenched by Cl^- (used for pH adjustment) under acidic conditions [1,65], efficient degradation of the organic compounds were still achieved. This suggests that the non-radical oxidation may play a role in the PDS/rGO-Ag^0/Fe_3O_4 system. In contrast, a higher substrate-dependent reactivity (*i.e.*, a significant reduction in k_{ini} of naproxen and BPA) at higher pH values accounted for the

reduced $SO_4^{\cdot -}$ conversion into ·OH (Eq. (7)) in PDS/rGO-Ag^0/Fe_3O_4 system. This indicates that $SO_4^{\cdot -}$ are considered as the dominant radical species apart from non-radical pathway and had a better selectivity toward naproxen and BPA under acidic conditions. To better identify the activities of oxidative degradation in catalytic removal of organic pollutants, the adsorption capacity of rGO-Ag^0/Fe_3O_4 for various organic compounds and the scavenging effect on free radical species should be studied further at different pH values.

3.5. Mechanism of PDS activation by rGO-Ag^0/Fe_3O_4 NH

Excess oxidant scavenger that may rapidly quench free $SO_4^{\cdot -}$ and ·OH in the aqueous suspension was used to shed light on the contribution of free reactive radicals to the oxidative degradation of phenol in a PDS/rGO-Ag^0/Fe_3O_4 system (Fig. 7). Methanol was used for its $SO_4^{\cdot -}$ and ·OH scavenging activity, and SRHA and SRFA were used to test natural organic matter (NOM), rich in electrons, as a radical scavenger[66]. Methanol is a well-known oxidant scavenger that shows ~300 times less reactivity with $SO_4^{\cdot -}$ than ·OH [67]. Interestingly, the hydrophilic methanol (methanol:PDS molar ratio of 100:1) significantly decreased the oxidation efficiency (from 47% without scavengers to 17% with 100 mM of methanol) by dramatically scavenging free $SO_4^{\cdot -}$ and ·OH (> 80% of inhibition after 6 h of reaction) formed during the reaction under neutral conditions (pH 7). The catalytic phenol removal decreased, to 41 and 26% at pH 7, in the presence of 10 mg/L SRHA and SRFA, respectively. This indicates that SRHA and SRFA can also quench phenol degradation (12.8 and 44.7% of inhibition after 6 h of reaction, respectively) in a PDS/rGO-Ag^0/Fe_3O_4 system due to the competing reactions of NOM with $SO_4^{\cdot -}$ and ·OH. Our previous study has shown that SRHA full of -COOH, -OH, and -NH_2 functional groups is weakly bound to rGO-Ag^0/Fe_3O_4 NH [43]. This suggests that the higher amount of (free) SRHA remaining in suspension resulted in much less impact on radical scavenging activity. The competitive reactions of radical scavengers (methanol and NOM) with $SO_4^{\cdot -}$ and ·OH inhibited the removal efficiency for phenol, but partial degradation of phenol could still be achieved via a non-radical oxidative pathway or ·OH converted from $SO_4^{\cdot -}$. However, further study is necessary to examine the type of oxidizing radical species involved or any non-radical oxidative pathway responsible for the degradation of phenol in PDS/rGO NH system. For example, *tert*-butyl alcohol (t-BuOH) may further inhibit the catalytic degradation via free ·OH formation [68]. The connected structure of rGO with Ag^0 and Fe_3O_4 NPs may facilitate an electron transfer from phenol (electron donor) to PDS while rGO can serve as an electron-transfer mediator [69].

4. Conclusions

rGO-Ag^0/Fe_3O_4 NH was prepared by deposition of Ag^0 and Fe_3O_4 NPs on rGO via *in situ* nucleation and crystallization. The NH showed a higher adsorption capacity of phenol than that of other single NPs (AgNP, NZVI, and rGO) at all pH values examined and could efficiently oxidize phenol in the heterogeneous activation of PDS. The catalytic performance of rGO-Ag^0/Fe_3O_4 was higher under acidic conditions, and PDS/rGO-Ag^0/Fe_3O_4 coupled process played a more dominant role in the oxidative degradation of phenol than H_2O_2/rGO-Ag^0/Fe_3O_4 coupled process. The mechanistic study showed the synergistic effects between the adsorption and catalytic oxidation on NH for phenol removal. The enhanced

performance of adsorption and oxidation of rGO-Ag^0/Fe_3O_4 could be attributable to the incorporation of rGO with individual NPs (i.e., Ag^0 and Fe_3O_4), promoting reactive sites for adsorption, catalytic oxidation, and electron transfer processes, oxidizing phenol via a non-radical oxidative pathway on the NH surface. Various organic pollutants were also tested to gain a better understanding of the selectivity of rGO-Ag^0/Fe_3O_4 under different pH conditions. Promisingly, more than 99% of the acetaminophen and E2 were removed in PDS/rGO-Ag^0/Fe_3O_4 system within 1 h of reaction at a neutral pH. As the solution pH increased, the reduced $SO_4\cdot^-$, due to recombination with ·OH, significantly decreased the removal efficiency of naproxen and BPA. This excellent magnetically-separable nanocatalyst may be a potential alternative in the oxidation of various organic compounds, preventing secondary pollution. Further research should be conducted to gain a better understanding of its reusability and possible degradation pathway of phenol prior to the practical application of this heterogeneous PDS/rGO-Ag^0/Fe_3O_4 system.

Supplementary Material

Refer to Web version on PubMed Central for supplementary material.

Acknowledgments

This study was funded by the U.S. Environmental Protection Agency and the Korea Ministry of Environment, ‘GAIA Project, 2015000540003′. This article has been reviewed in accordance with

U.S. Environmental Protection Agency policy and approved for publication. However, the research results do not necessarily reflect the views or policies, and no official endorsement should be inferred.

References

1. Antoniou MG, Armah A, Dionysiou DD, Degradation of microcystin-LR using sulfate radicals generated through photolysis, thermolysis and e-transfer mechanisms, Appl. Catal. B 96 (2010) 290–298.
2. Avetta P, Pensato A, Minella M, Malandrino M, Maurino V, Minero C, Hanna K, Vione D, Activation of persulfate by irradiated magnetite: implications for the degradation of phenol under heterogeneous photo-Fenton-like conditions, Environ. Sci. Technol 49 (2014) 1043–1050.
3. Zou J, Ma J, Chen L, Li X, Guan Y, Xie P, Pan C, Rapid acceleration of ferrous iron/peroxymonosulfate oxidation of organic pollutants by promoting Fe (III)/Fe(II) cycle with hydroxylamine, Environ. Sci. Technol 47 (2013) 11685–11691. [PubMed: 24033112]
4. Zeng T, Zhang X, Wang S, Niu H, Cai Y, Spatial confinement of a Co3O4 catalyst in hollow metal–organic frameworks as a nanoreactor for improved degradation of organic pollutants, Environ. Sci. Technol 49 (2015) 2350–2357. [PubMed: 25608052]
5. Deng J, Shao Y, Gao N, Deng Y, Zhou S, Hu X, Thermally activated persulfate (TAP) oxidation of antiepileptic drug carbamazepine in water, Chem. Eng. J 228 (2013) 765–771.
6. Hazime R, Nguyen Q, Ferronato C, Huynh T, Jaber F, Chovelon J-M, Optimization of imazalil removal in the system UV/TiO2/K2S2O8 using a response surface methodology (RSM), Appl. Catal. B 132 (2013) 519–526.
7. Li B, Li L, Lin K, Zhang W, Lu S, Luo Q, Removal of 1, 1, 1-trichloroethane from aqueous solution by a sono-activated persulfate process, Ultrason. Sonochem 20 (2013) 855–863. [PubMed: 23266439]
8. Liu N, Xu G, Wu M, He X, Tang L, Shi W, Wang L, Shao H, Radical-induced destruction of diethyl phthalate in aqueous solution: kinetics, spectral properties, and degradation efficiencies studies, Res. Chem. Intermed 39 (2013) 3727–3737.

9. Anipsitakis GP, Dionysiou DD, Radical generation by the interaction of transition metals with common oxidants, Environ. Sci. Technol 38 (2004) 3705–3712. [PubMed: 15296324]
10. Liang C, Guo Y-Y, Chien Y-C, Wu Y-J, Oxidative degradation of MTBE by pyrite-activated persulfate: proposed reaction pathways, Ind. Eng. Chem. Res 49 (2010) 8858–8864.
11. Yan J, Lei M, Zhu L, Anjum MN, Zou J, Tang H, Degradation of sulfamonomethoxine with Fe3O4 magnetic nanoparticles as heterogeneous activator of per-sulfate, J. Hazard. Mater 186 (2011) 1398–1404. [PubMed: 21237557]
12. Zhu L, Ai Z, Ho W, Zhang L, Core–shell Fe–Fe2O3 nanostructures as effective persulfate activator for degradation of methyl orange, Sep. Purif. Technol 108 (2013) 159–165.
13. Bai S, Shen X, Zhong X, Liu Y, Zhu G, Xu X, Chen K, One-pot solvothermal preparation of magnetic reduced graphene oxide-ferrite hybrids for organic dye removal, Carbon 50 (2012) 2337–2346.
14. Hussain I, Zhang Y, Huang S, Du X, Degradation of p-chloroaniline by persulfate activated with zero-valent iron, Chem. Eng. J 203 (2012) 269–276.
15. Ghauch A, Ayoub G, Naim S, Degradation of sulfamethoxazole by persulfate assisted micrometric Fe0 in aqueous solution, Chem. Eng. J 228 (2013) 1168–1181.
16. Wang Y, Cheng R, Wen Z, Zhao L, Synthesis and characterization of single-crystalline MnFe2O4 ferrite nanocrystals and their possible application in water treatment, Eur. J. Inorg. Chem 2011 (2011) 2942–2947.
17. Sun H, Kwan C, Suvorova A, Ang HM, Tadé MO, Wang S, Catalytic oxidation of organic pollutants on pristine and surface nitrogen-modified carbon nanotubes with sulfate radicals, Appl. Catal. B 154 (2014) 134–141.
18. Lee H, Lee H-J, Jeong J, Lee J, Park N-B, Lee C, Activation of persulfates by carbon nanotubes: oxidation of organic compounds by nonradical mechanism, Chem. Eng. J 266 (2015) 28–33.
19. Shi P, Su R, Zhu S, Zhu M, Li D, Xu S, Supported cobalt oxide on graphene oxide: highly efficient catalysts for the removal of Orange II from water, J. Hazard. Mater 229 (2012) 331–339. [PubMed: 22738772]
20. Peng W, Liu S, Sun H, Yao Y, Zhi L, Wang S, Synthesis of porous reduced graphene oxide as metal-free carbon for adsorption and catalytic oxidation of organics in water, J. Mater. Chem. A 1 (2013) 5854–5859.
21. Sun H, Liu S, Zhou G, Ang HM, Tadé MO, Wang S, Reduced graphene oxide for catalytic oxidation of aqueous organic pollutants, ACS Appl. Mater. Interfaces 4 (2012) 5466–5471. [PubMed: 22967012]
22. Upadhyay RK, Soin N, Roy SS, Role of graphene/metal oxide composites as photocatalysts, adsorbents and disinfectants in water treatment: a review, RSC Adv. 4 (2014) 3823–3851.
23. Wang Z, Xu C, Gao G, Li X, Facile synthesis of well-dispersed Pd–graphene nanohybrids and their catalytic properties in 4-nitrophenol reduction, RSC Adv. 4 (2014) 13644–13651.
24. Yao Y, Miao S, Liu S, Ma LP, Sun H, Wang S, Synthesis, characterization, and adsorption properties of magnetic Fe3O4@graphene nanocomposite, Chem. Eng. J 184 (2012) 326–332.
25. Yang S, Yue W, Zhu J, Ren Y, Yang X, Graphene-based mesoporous SnO2 with enhanced electrochemical performance for lithium-ion batteries, Adv. Funct. Mater 23 (2013) 3570–3576.
26. Lee E, Hong J-Y, Kang H, Jang J, Synthesis of TiO2 nanorod-decorated graphene sheets and their highly efficient photocatalytic activities under visible-light irradiation, J. Hazard. Mater 219 (2012) 13–18. [PubMed: 22497717]
27. Al-Anazi A, Abdelraheem WH, Han C, Nadagouda MN, Sygellou L, Arfanis MK, Falaras P, Sharma VK, Dionysiou DD, Cobalt ferrite nanoparticles with controlled composition-peroxymonosulfate mediated degradation of 2-phenylbenzimidazole-5-sulfonic acid, Appl. Catal. B 221 (2018) 266–279.
28. Hu G, Tang B, Photocatalytic mechanism of graphene/titanate nanotubes photocatalyst under visible-light irradiation, Mater. Chem. Phys 138 (2013) 608–614.
29. Fu D, Han G, Chang Y, Dong J, The synthesis and properties of ZnO–graphene nano hybrid for photodegradation of organic pollutant in water, Mater. Chem. Phys 132 (2012) 673–681.
30. Yusoff N, Huang N, Muhamad M, Kumar S, Lim H, Harrison I, Hydrothermal synthesis of CuO/functionalized graphene nanocomposites for dye degradation, Mater. Lett 93 (2013) 393–396.

31. Gao Z, Liu J, Xu F, Wu D, Wu Z, Jiang K, One-pot synthesis of graphene–cuprous oxide composite with enhanced photocatalytic activity, Solid State Sci. 14 (2012) 276–280.
32. Fu Y, Wang X, Magnetically separable ZnFe2O4–graphene catalyst and its high photocatalytic performance under visible light irradiation, Ind. Eng. Chem. Res 50 (2011) 7210–7218.
33. Xia J, Di J, Yin S, Xu H, Zhang J, Xu Y, Xu L, Li H, Ji M, Facile fabrication of the visible-light-driven Bi2WO6/BiOBr composite with enhanced photocatalytic activity, RSC Adv. 4 (2014) 82–90.
34. Yao Y, Xu C, Yu S, Zhang D, Wang S, Facile synthesis of Mn3O4–reduced graphene oxide hybrids for catalytic decomposition of aqueous organics, Ind. Eng. Chem. Res 52 (2013) 3637–3645.
35. Yao Y, Yang Z, Sun H, Wang S, Hydrothermal synthesis of Co3O4–graphene for heterogeneous activation of peroxymonosulfate for decomposition of phenol, Ind. Eng. Chem. Res 51 (2012) 14958–14965.
36. Yao Y, Xu C, Miao S, Sun H, Wang S, One-pot hydrothermal synthesis of Co(OH) 2 nanoflakes on graphene sheets and their fast catalytic oxidation of phenol in liquid phase, J. Colloid Interface Sci 402 (2013) 230–236. [PubMed: 23643184]
37. Yao Y, Cai Y, Lu F, Wei F, Wang X, Wang S, Magnetic recoverable MnFe2O4 and MnFe2O4-graphene hybrid as heterogeneous catalysts of peroxymonosulfate activation for efficient degradation of aqueous organic pollutants, J. Hazard. Mater 270 (2014) 61–70. [PubMed: 24548886]
38. Yao Y, Yang Z, Zhang D, Peng W, Sun H, Wang S, Magnetic CoFe2O4–graphene hybrids: facile synthesis, characterization, and catalytic properties, Ind. Eng. Chem. Res 51 (2012) 6044–6051.
39. Conley JM, Symes SJ, Schorr MS, Richards SM, Spatial and temporal analysis of pharmaceutical concentrations in the upper Tennessee River basin, Chemosphere 73 (2008) 1178–1187. [PubMed: 18774586]
40. Godfrey E, Woessner WW, Benotti MJ, Pharmaceuticals in on-site sewage effluent and ground water, Western Montana, Ground Water 45 (2007) 263–271. [PubMed: 17470115]
41. Benotti MJ, Trenholm RA, Vanderford BJ, Holady JC, Stanford BD, Snyder SA, Pharmaceuticals and endocrine disrupting compounds in US drinking water, Environ. Sci. Technol 43 (2008) 597–603.
42. Shen R, Andrews SA, Demonstration of 20 pharmaceuticals and personal care products (PPCPs) as nitrosamine precursors during chloramine disinfection, Water Res. 45 (2011) 944–952. [PubMed: 20950838]
43. Park CM, Wang D, Heo J, Her N, Su C, Aggregation of reduced graphene oxide and its nanohybrids with magnetite and elemental silver under environmentally relevant conditions, Sci. Total Environ (2017) (under review).
44. Chen C, Yang QH, Yang Y, Lv W, Wen Y, Hou PX, Wang M, Cheng HM, Self-assembled free-standing graphite oxide membrane, Adv. Mater 21 (2009) 3007–3011.
45. Bari VR, Dhorda U, Sundaresan M, A simultaneous packed column supercritical fluid chromatographic method for ibuprofen, chlorzoxazone and acetaminophen in bulk and dosage forms, Talanta 45 (1997) 297–302. [PubMed: 18967006]
46. Stankovich S, Dikin DA, Dommett GH, Kohlhaas KM, Zimney EJ, Stach EA, Piner RD, Nguyen ST, Ruoff RS, Graphene-based composite materials, Nature 442 (2006) 282–286. [PubMed: 16855586]
47. Liu W, Ma J, Shen C, Wen Y, Liu W, A pH-responsive and magnetically separable dynamic system for efficient removal of highly dilute antibiotics in water, Water Res. 90 (2016) 24–33. [PubMed: 26724436]
48. Bandyopadhyay R, Selbo J, Amidon GE, Hawley M, Application of powder X-ray diffraction in studying the compaction behavior of bulk pharmaceutical powders, J. Pharm. Sci 94 (2005) 2520–2530. [PubMed: 16200547]
49. Yang H, Yan R, Chen H, Lee DH, Zheng C, Characteristics of hemicellulose, cellulose and lignin pyrolysis, Fuel 86 (2007) 1781–1788.
50. Yang S-T, Chang Y, Wang H, Liu G, Chen S, Wang Y, Liu Y, Cao A, Folding/aggregation of graphene oxide and its application in Cu2+ removal, J. Colloid Interface Sci 351 (2010) 122–127. [PubMed: 20705296]

51. Hoag GE, Collins JB, Holcomb JL, Hoag JR, Nadagouda MN, Varma RS, Degradation of bromothymol blue by 'greener' nano-scale zero-valent iron synthesized using tea polyphenols, J. Mater. Chem 19 (2009) 8671–8677.
52. Mahitha B, Raju BDP, Dillip G, Reddy CM, Mallikarjuna K, Manoj L, Priyanka S, Rao KJ, Sushma NJ, Biosynthesis, characterization and antimicrobial studies of AgNPs extract from Bacopa monniera whole plant, Dig. J. Nanomater. Biostruct 6 (2011) 135–142.
53. Hartono T, Wang S, Ma Q, Zhu Z, Layer structured graphite oxide as a novel adsorbent for humic acid removal from aqueous solution, J. Colloid Interface Sci 333 (2009) 114–119. [PubMed: 19233379]
54. Heo Y, Im H, Kim J, The effect of sulfonated graphene oxide on sulfonated poly (ether ketone) membrane for direct methanol fuel cells, J. Membr. Sci 425 (2013) 11–22.
55. Jiang P, Li SY, Xie SS, Gao Y, Song L, Machinable long PVP-stabilized silver nanowires, Chem. Eur. J 10 (2004) 4817–4821. [PubMed: 15372648]
56. Singhal R, Samariya A, Kumar S, Sharma S, Xing Y, Deshpande U, Shripathi T, Saitovitch E, A close correlation between induced ferromagnetism and oxygen deficiency in Fe doped In2O3, Appl. Surf. Sci 257 (2010) 1053–1057.
57. Qi C, Liu X, Ma J, Lin C, Li X, Zhang H, Activation of peroxymonosulfate by base: implications for the degradation of organic pollutants, Chemosphere 151 (2016) 280–288. [PubMed: 26946115]
58. Liang C, Su H-W, Identification of sulfate and hydroxyl radicals in thermally activated persulfate, Ind. Eng. Chem. Res 48 (2009) 5558–5562.
59. Mokhtari SA, Farzadkia M, Esrafili A, Kalantari RR, Jafari AJ, Kermani M, Gholami M, Bisphenol A removal from aqueous solutions using novel UV/persulfate/H2O2/Cu system: optimization and modelling with central composite design and response surface methodology, J. Environ. Health Sci. Eng 14 (2016) 19. [PubMed: 27980792]
60. Ho Y-S, McKay G, Pseudo-second order model for sorption processes, Process Biochem. 34 (1999) 451–465.
61. Park CM, Han J, Chu KH, Al-Hamadani YA, Her N, Heo J, Yoon Y, Influence of solution pH, ionic strength, and humic acid on cadmium adsorption onto activated biochar: experiment and modeling, J. Ind. Eng. Chem 48 (2017) 186–193.
62. Wang X, Huang S, Zhu L, Tian X, Li S, Tang H, Correlation between the ad-sorption ability and reduction degree of graphene oxide and tuning of adsorption of phenolic compounds, Carbon 69 (2014) 101–112.
63. Park CM, Heo J, Yoon Y, Oxidative degradation of bisphenol A and 17α-ethinylestradiol by Fenton-like activity of silver nanoparticles in aqueous solution, Chemosphere 168 (2017) 617–622. [PubMed: 27838031]
64. Ntsendwana B, Mamba B, Sampath S, Arotiba O, Electrochemical detection of bisphenol A using graphene-modified glassy carbon electrode, Int. J. Electrochem. Sci 7 (2012) 3501–3512.
65. Duan X, Ao Z, Zhou L, Sun H, Wang G, Wang S, Occurrence of radical and nonradical pathways from carbocatalysts for aqueous and nonaqueous catalytic oxidation, Appl. Catal. B 188 (2016) 98–105.
66. Keenan CR, Sedlak DL, Factors affecting the yield of oxidants from the reaction of nanoparticulate zero-valent iron and oxygen, Environ. Sci. Technol 42 (2008) 1262–1267. [PubMed: 18351103]
67. Khan JA, He X, Shah NS, Khan HM, Hapeshi E, Fatta-Kassinos D, Dionysiou DD, Kinetic and mechanism investigation on the photochemical de-gradation of atrazine with activated H2O2, S2O82- and HSO5-, Chem. Eng. J 252 (2014) 393–403.
68. He X, Armah A, O'Shea KE, Dionysiou DD, Kinetics and mechanisms of cylindrospermopsin destruction by sulfate radical-based advanced oxidation processes, Water Res. 63 (2014) 168–178. [PubMed: 25000199]
69. Li D, Duan X, Sun H, Kang J, Zhang H, Tade MO, Wang S, Facile synthesis of nitrogen-doped graphene via low-temperature pyrolysis: the effects of precursors and annealing ambience on metal-free catalytic oxidation, Carbon 115 (2017) 649

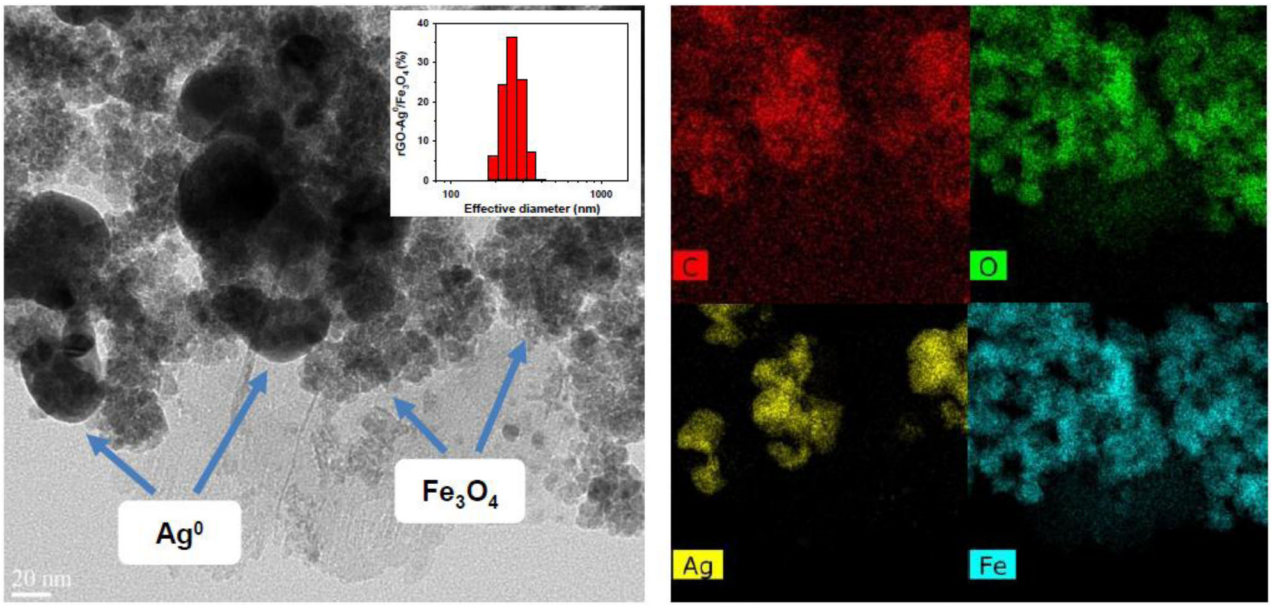

Fig. 1.

FE-TEM micrograph, particle size distribution (inserted figure) of rGO-Ag^0/Fe_3O_4 NH (left panel), and its elemental mapping results for C, O, Ag, and Fe right panel).

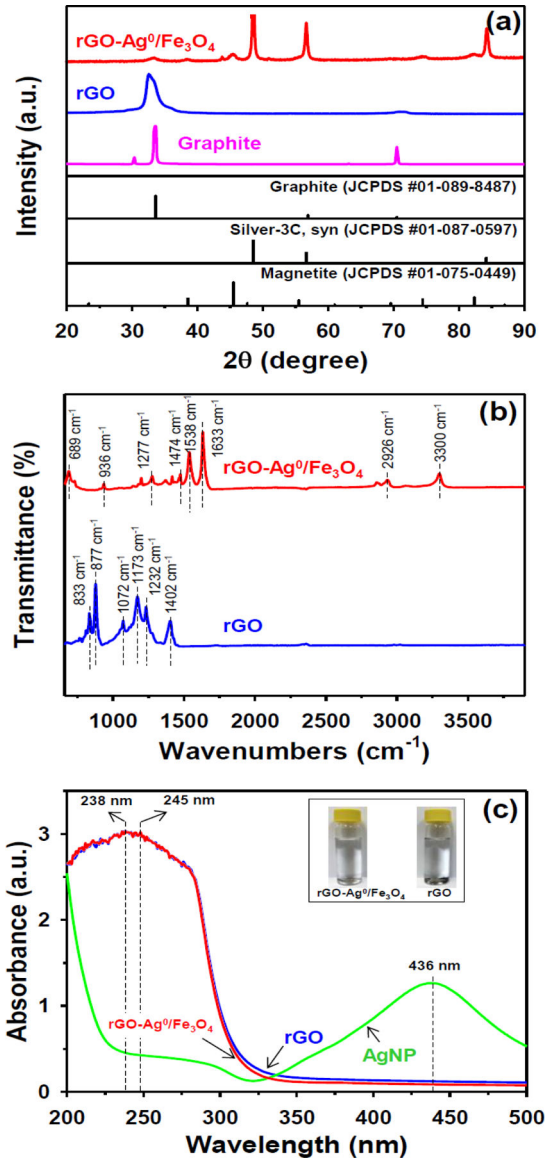

Fig. 2.

(a) XRD patterns, (b) FT-IR spectra, and (c) UV–vis absorption spectra of rGO, AgNP, and rGO-Ag^0/Fe_3O_4 NH.

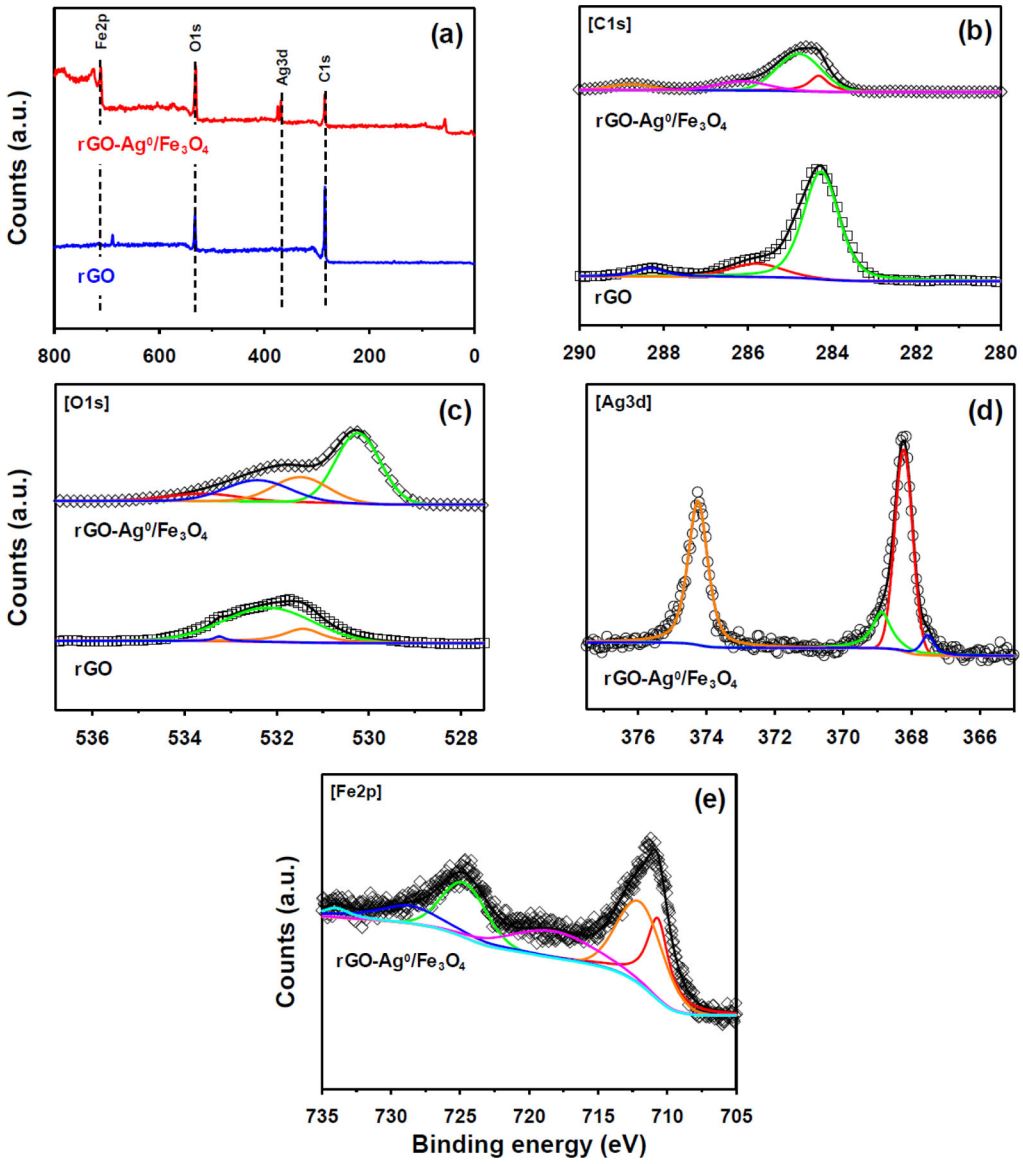

Fig. 3.

X-ray photoelectron spectra of (a) wide survey scan and deconvolution, (b) C1s, (c) O1s, (d) Ag3d, and (e) Fe2p spectra of rGO and rGO-Ag^0/Fe_3O_4 NH.

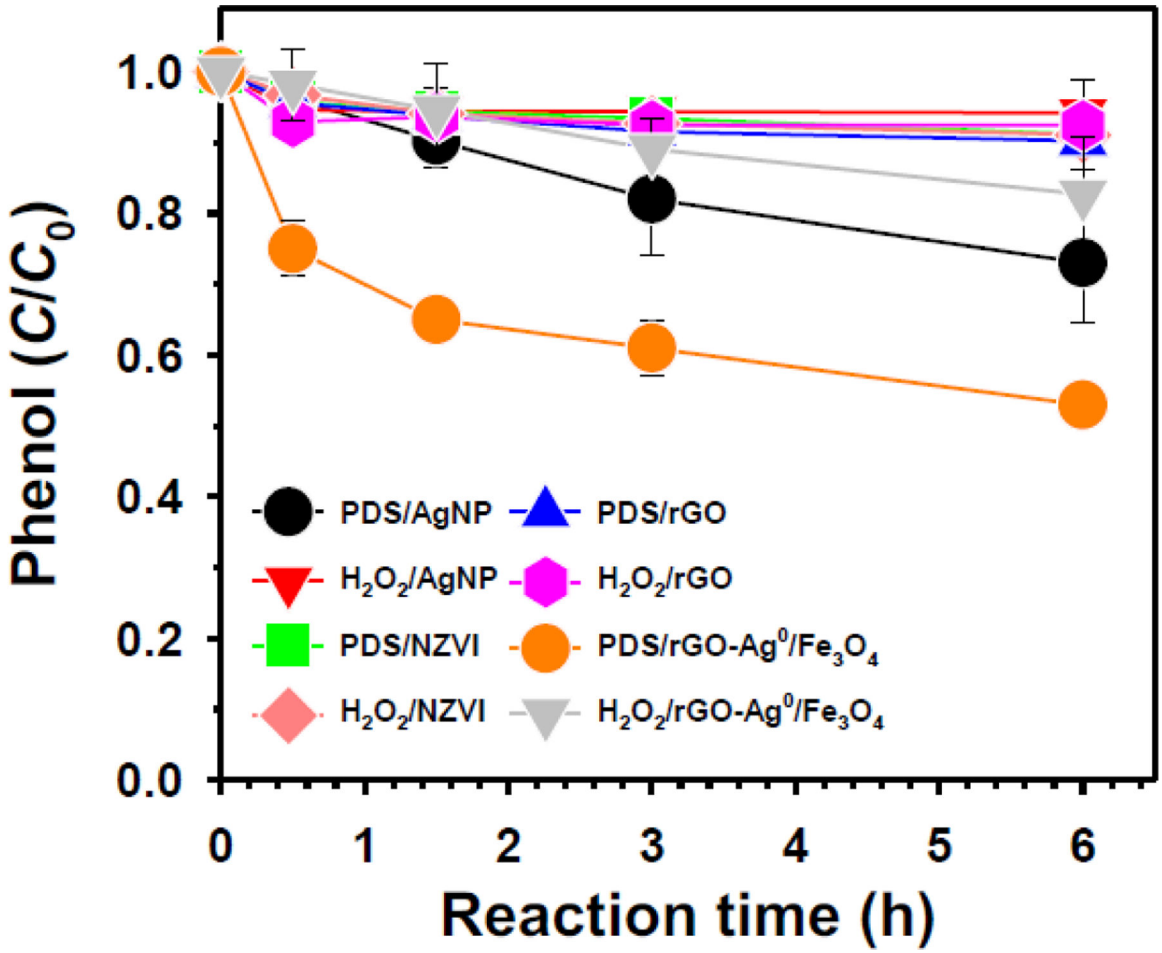

Fig. 4.

Removal of phenol by AgNP, NZVI, rGO and rGO-Ag^0/Fe_3O_4 NH in catalytic activation of PDS and H_2O_2. Experimental conditions: $[AgNP]_0 = [NZVI]_0 = [rGO]_0 = [rGO\text{-}Ag^0/Fe_3O_4]_0$ = 0.1 g/L; $[phenol]_0$ = 10 μM; $[PDS]_0 = [H_2O_2]_0$ = 1 mM; pH = 7; and temperature = 298 K.

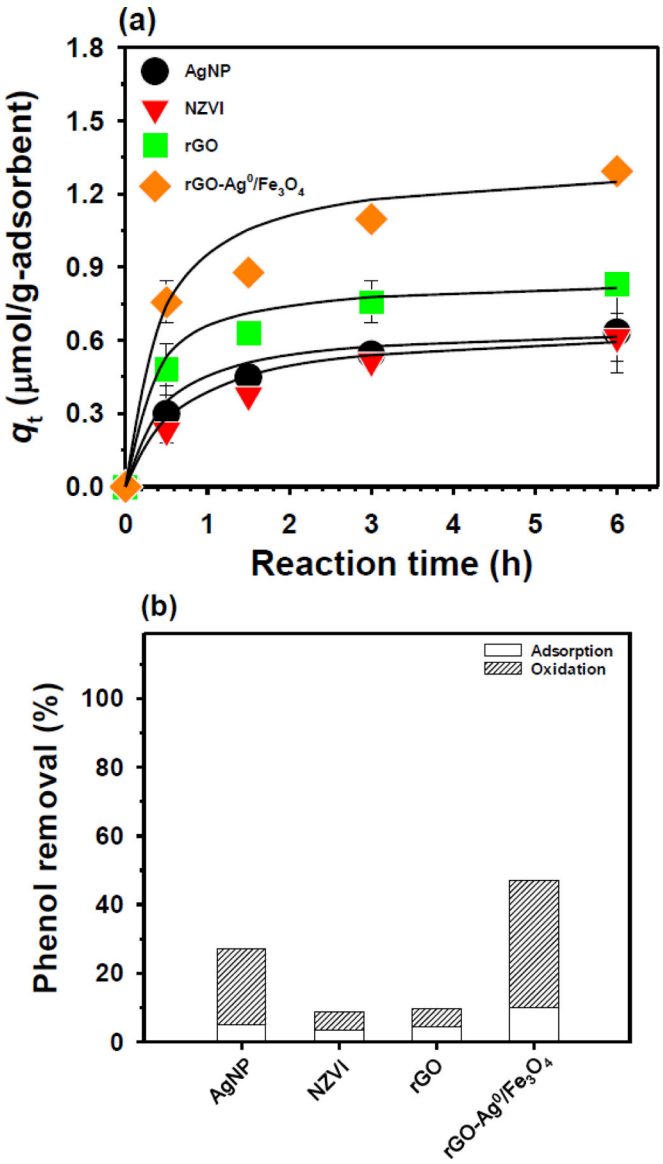

Fig. 5.

(a) Adsorptive removal of phenol by AgNP, NZVI, rGO and rGO-Ag^0/Fe_3O_4 NH. Solid lines are calculated from nonlinear least square regression of the adsorption data according to pseudo-second-order kinetic model. (b) Adsorptive removal and oxidative degradation of phenol after 6 h of reaction. The oxidation was only counted for the un-adsorbed fraction of phenol after 6 h of adsorption experiments. Experimental conditions: [AgNP] = [NZVI] = $[rGO]_0$ = $[rGO\text{-}Ag^0/Fe_3O_4]_0$ = 0.1 g/L; $[phenol]_0$ = 10 μM; pH = 7; and temperature = 298 K.

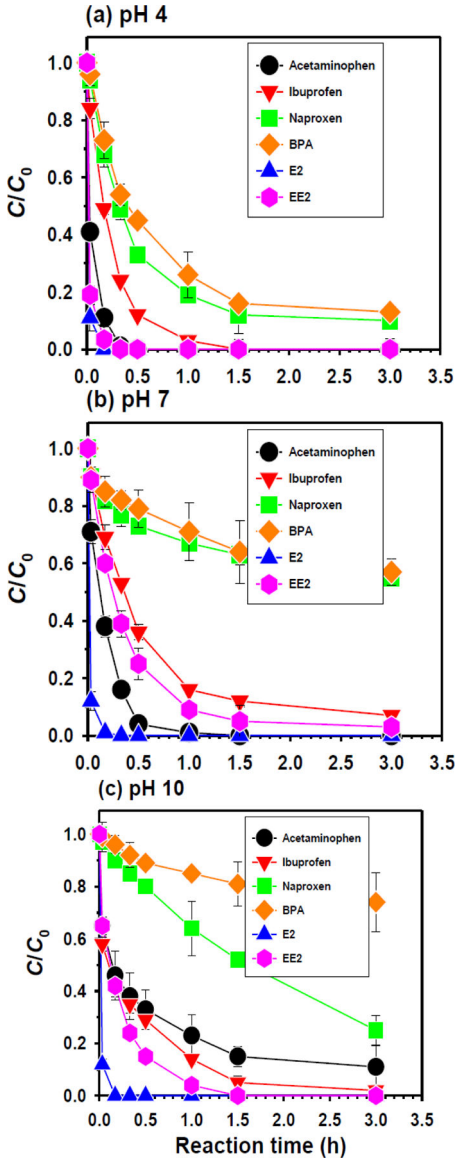

Fig. 6.

Removal of acetaminophen, ibuprofen, naproxen, BPA, E2, and EE2 by rGO-Ag^0/Fe_3O_4 NH in catalytic activation of PDS. Experimental conditions: [rGO-Ag^0/Fe_3O_4]$_0$ = 0.1 g/L; [acetaminophen]$_0$ = [ibuprofen]$_0$ = [naproxen]$_0$ = [BPA]$_0$ = [E2] = [EE2] = 10 μM; [PDS]$_0$ = 1 mM; pH = 4, 7, and 10; and temperature = 298 K.

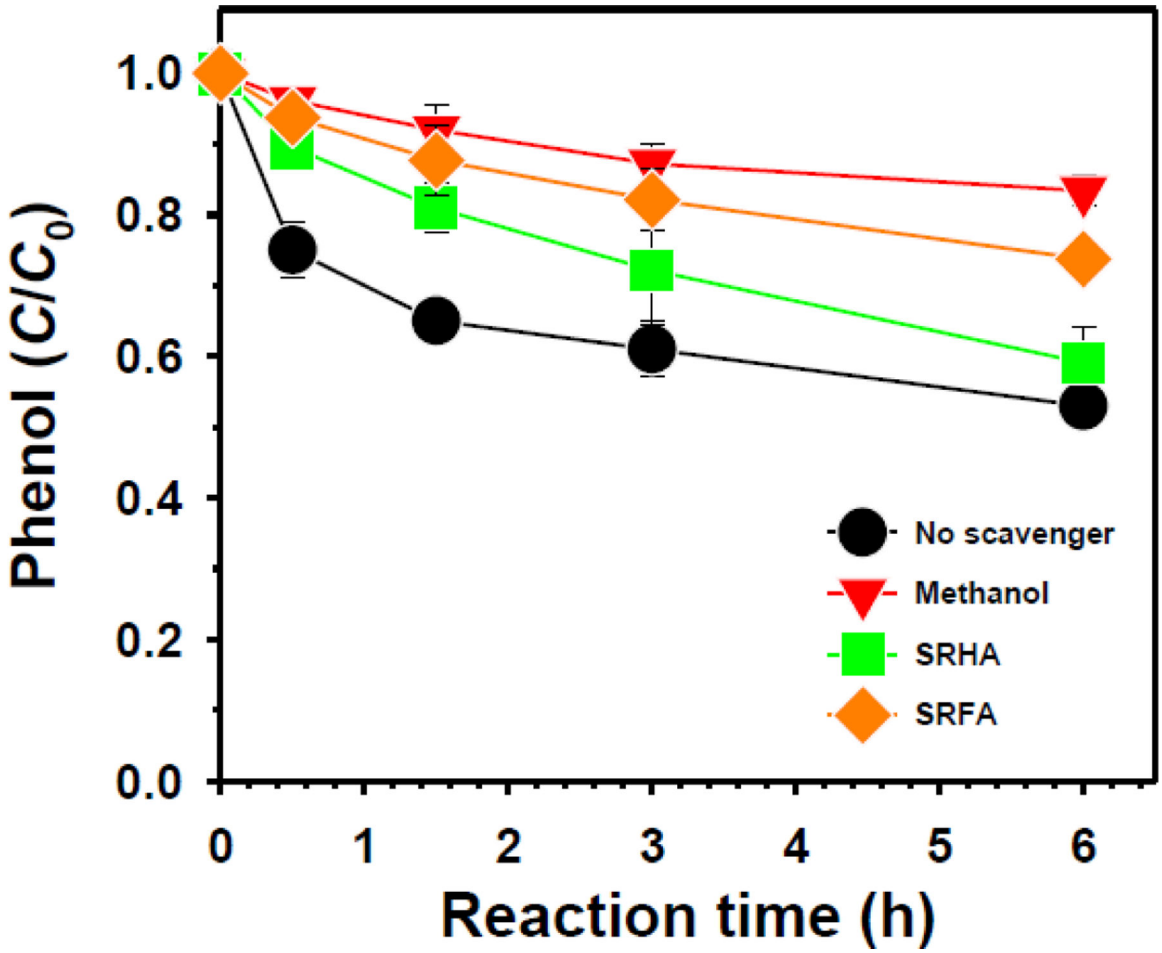

Fig. 7.

Removal of phenol in PDS/GO–Ag^0/Fe_3O_4 system in the presence of reactive oxidant scavenger [methanol and natural organic matter (SRHA and SRFA)]. Experimental conditions: $[rGO\text{-}Ag^0/Fe_3O_4]_0$ = 0.1 g/L; $[phenol]_0$ = 10 μM; $[PDS]_0$ = 1 mM; [Methanol] = 100 mM; [SRHA] = [SRFA] = 10 mg/L; pH = 7; and temperature = 298 K.